Soft magneto-sensitive elastomer and polyvinylidene fluoride polymer based nonlinear piezoelectric energy harvesting: design, modelling and experiment

Soft Magneto-Sensitive Elastomer and Polyvinylidene Fluoride Polymer Based Nonlinear Piezoelectric Energy Harvesting: Design, Modelling and Experiment

Zhaoshu Yang[1], Lihua Tang[1*], Mengying Xie[2], Shuaishuai Sun[3], Weihua Li[3], Kean Aw[1]

1. Dept. Mechanical Engineering, University of Auckland, New Zealand, 1010

2. Ritsumeikan Global Innovation Research Organization, Ritsumeikan University, Shiga, Japan, 525-8577

3. School of Mechanical, Materials and Mechatronic Engineering, University of Wollongong, Australia, New South Wales 2522

Abstract

In this paper, a broadband vibrational energy harvester (VEH) is developed based on a soft magneto-sensitive elastomer (SMSE). The utilization of SMSE provides the VEH with a strong softening effect when it is subjected to the magnetic field of a permanent magnet. A polyvinylidene fluoride (PVDF) layer is attached to the SMSE to convert vibrational energy into electricity. A magneto-electro-mechanical model based on finite element method is developed and is further reduced using assumed modes. Two prototypes are fabricated with different SMSE thicknesses (3 mm and 5 mm respectively). Frequency sweep experiments are conducted to investigate their broadband behavior. The difference between jumping frequencies are 2.39 Hz and 4.34 Hz at a low acceleration level of 0.3 g. With the broadband characteristics of SMSE, the two prototypes are capable of providing power over a wide frequency range and generating an average power of 0.096 μW and 0.11 μW respectively with a load of 4.7 MΩ.

Key words: Magnetic polymer; Energy harvesting; PVDF; Nonlinear analysis; frequency bandwidth;

1. Introduction

Vibration Energy Harvester (VEH) is an electromechanical device that can harvest and convert ambient vibrational energy into electricity. This technology is believed to be a promising alternative energy source to conventional batteries and has the potential to deliver sustainable energy to supply low-power wearable electronics [1, 2].

---

* Corresponding Author, email: l.tang@auckland.ac.nz

In recent years, VEH in low frequency domain has become an attractive research topic [3-6], as large amount of environmental vibrations, like human body movements, are usually confined in the low frequency spectra [7-9]. Predominant VEHs to date can only achieve an acceptable energy conversion efficiency around their resonances [10]. The metal substrates of the traditional VEHs and the requirement of miniaturization for wearable devices means that a low resonant frequency is challenging [11, 12]. This poses a problem to match the frequencies to maximize the efficiency of VEHs.

Due to the above limitation, attention has been given to the techniques aiming at broadening the operating bandwidth of low frequency VEHs. Yang and Towfighian proposed a nonlinear VEH with internal resonance [13]. The structure consists of two cantilevers with magnets on the tips. The frequency bandwidth could be broadened by the interaction between magnets and the internal resonance phenomenon. Leadenham and Erturk proposed an M-shaped broadband piezoelectric energy harvester [14]. Due to the specific shape of the beam, a nonlinear frequency response could be realized under 0.1 g excitation. Bendame et al. proposed a wideband, low-frequency springless VEHs [15]. The frequency bandwidth is broadened via the impacts between seismic mass and two mechanical stoppers.

Despite the diverse designs for low frequency energy harvesters, almost all of them were fabricated using metallic materials as substrates. The large densities of these materials pose a challenge for light-weight applications, for instance, VEHs for wearable devices. Using soft materials and structures could mitigate the above issue. Soft materials and structures possess low Young's modulus, which enables a VEH to resonate at a low frequency without increasing its weight or size. In addition, a large amplitude can be expected by using soft structures even with low excitations. This characteristic makes the soft structure a promising solution for light-weight applications subject to low accelerations at low frequency. Among all the soft materials, polyvinylidene fluoride (PVDF) is one type of piezoelectric polymer with a low Young's modulus. It is regarded as a promising candidate due to its high sensitivity [16], high maximum operational strain [17] and comparable electromechanical coupling [18]. Despite the diverse design of PVDF based VEHs, most of them are still linear oscillators based on metal substrates [18, 19] and suffer from the limited bandwidth around their linear resonances. To broaden the bandwidth of the PVDF based VEHs, Emad et al. developed a nonlinear hardening VEH based on clamped-clamped PVDF beam [20]. According to their simulation results, the frequency bandwidth broadened from 50 Hz to 70 Hz at an excitation level of 0.5 g. Li et al. prototyped a bi-resonant PVDF structure based VEH. The structure consisted of two cantilevers with

2

different resonant frequencies. The operating frequency bandwidth is broadened to 14 Hz at an acceleration of 1 g with the maximum output power of 0.35 μW [21].

In this paper, the soft magneto-sensitive elastomer (SMSE) is utilized as the substrate for a PVDF based VEH. Such a VEH device is termed as SMSE/PVDF-VEH. The SMSE is a very soft elastomer mixed with iron particles. When a permanent magnet (PM) is placed near the SMSE, the iron particles will interact with the PM magnetic field during vibration, making the whole elastomer behaves as a highly flexible magneto-sensitive material. These unique behaviours of the SMSE empower itself an obvious softening nonlinear effect. By integrating the SMSE, this work develops a VEH with considerable broad operation bandwidth in low frequency and low excitation conditions.

2. Design and Fabrication

2.1 Design Principle

In the reported nonlinear VEH structures, the nonlinear magnetic force is provided via the interaction of two permanent magnets (PMs): one fixed onto the base and the other at the tip of the cantilever. The cantilever is usually made of metal to support the PM at its free end [22-24].

The mechanism of the bandwidth broadening in the SMSE/PVDF-VEH is different from most reported nonlinear VEHs. Figure 1 (a) depicts the layout of the SMSE/PVDF-VEH. The proposed VEH consists of two main components: the SMSE/PVDF cantilever and the PM. The mechanism of the frequency broadening effect in the proposed design is shown in Figure 1 (b) and (c). Primarily, this effect derives from the uneven distribution of the PM's magnetic field. During vibration, the cantilever deforms and its free end deviates from the equilibrium position. Thus, its corresponding magnetic force decreases nonlinearly due to the sharp change in the magnetic field. This change in the horizontal component of the magnetic force is responsible for the corresponding variation of the equivalent stiffness, which eventually leads to softening behaviour. Different from other similar configurations using metal substrates [25, 26], SMSE enables the cantilever itself to interact with the external magnetic field. The overall structure is small, lightweight, and very flexible. Most importantly, this composite structure could achieve a pronounced softening effect at a very low acceleration level.

3

(a)   (b)   (c)
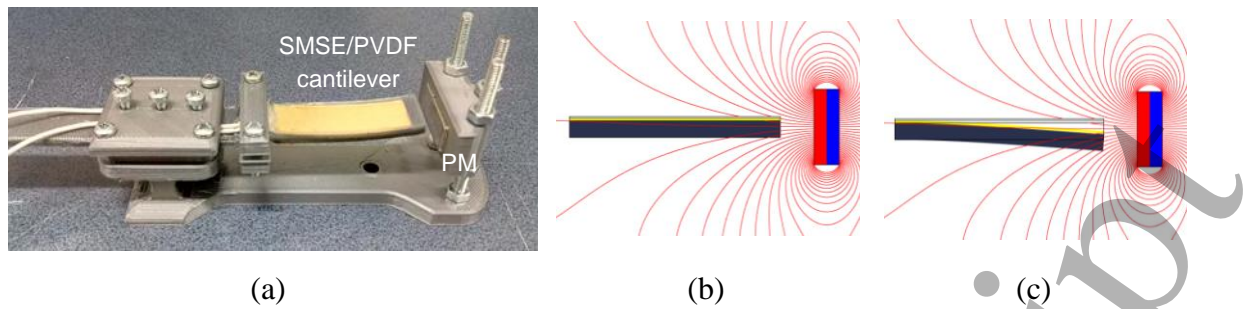
Figure 1. Layout of SMSE/PVDF-VEH and its bandwidth broadening principle, (a) layout of SMSE/PVDF-VEH; (b) Un-deformed SMSE/PVDF-VEH in a PM magnetic field; (c) Deformed SMSE/PVDF-VEH in a PM magnetic field

2.2 Fabrication Procedure

The fabrication procedure of the SMSE/PVDF cantilever is as follows: **Step 1**, Iron particles (Atomised231-096-4, Inoxia Inc.) were mixed evenly in an Eco-Flex resin (Ecoflex00-30, Smooth-on Corp.). **Step 2**, Put the mixture in a mold and then put the mold in a vacuum chamber overnight to fully degas and cure the sample. **Step 3,** a pair of conducting wires was attached to both sides of PVDF using silver paste (CW2400, CircuitWorks Corp.); **Step 4**, the PVDF layer was attached to the top of the SMSE layer, and then another thin layer of Eco-flex was attached on the top of the PVDF, to ensure a proper bonding between the PVDF and SMSE. Two prototypes were fabricated with the SMSE layers of two different thicknesses of SMSE. In Prototype 1, the SMSE layer thickness is 3 mm. In Prototype 2, the SMSE layer thickness is 5 mm. Two prototypes are shown in Figure 2.

(a)   (b)

Figure 2. (a) two prototypes of SMSE/PVDF-VEH and (b) their multi-layer structures

3. Magneto-Electro-Mechanical Modelling

In the modelling of piezoelectric composite cantilever VEHs, Wang and Tang considered a nonlinear two-DOFs (Degree of Freedom) system comprising a primary cantilever and a parasitic cantilever [25]. The nonlinearity is introduced by the magnetic force and modelled

4

with magnetic dipole-dipole interaction, which, however, cannot be applied in our SMSE/PVDF cantilever. This is because the dipole-dipole model neglects the geometrical s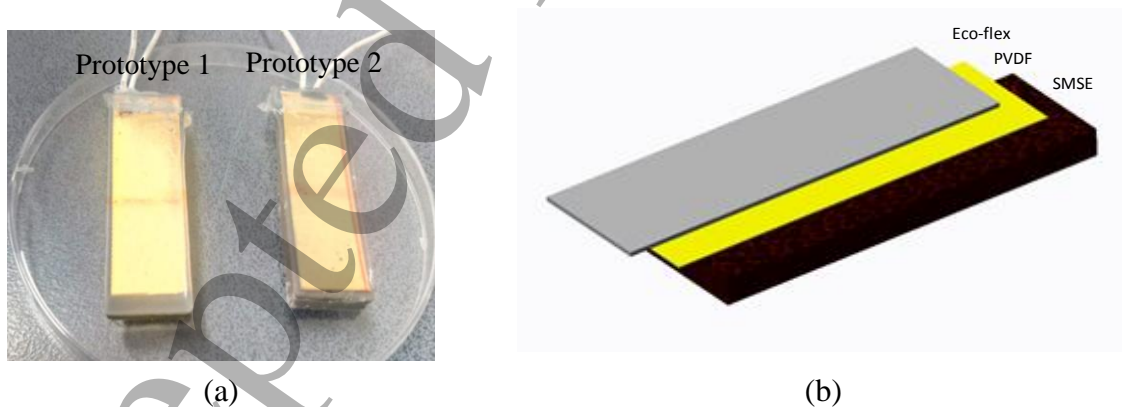hape of PM. However, the geometrical shape of the magnet proved to be important to our SMSE/PVDF cantilever as the SMSE is highly magneto-sensitive. Ferrari et al. developed a VEH using ferromagnetic cantilever as the substrate of a piezoelectric bimorph. In their model, the ferromagnetic cantilever is treated as a single DOF system. The magnetic field generated by the PM is pre-calculated using Comsol Multiphysics and approximated as a 3rd order polynomial function [27]. Their model cannot be applied in this SMSE/PVDF cantilever because the single DOF model cannot take into consideration the magnetic force distribution along the cantilever. Due to the high magneto-sensitivity of the SMSE substrate, the magnetic field distribution of PM with specific shape and dimensions have to be properly modelled, where both the horizontal and vertical distribution of the magnetic force along the magneto-sensitive cantilever should be considered.

3.1 Magnetic Field

The coordinate system used in the modelling of the SMSE/PVDF cantilever is shown in Figure 3. The clamping position of the cantilever is assumed as the origin. The x-direction is along the longitudinal axis of the cantilever pointing to the free end and the y-direction is along the direction of the deflection of the cantilever.

Figure 3. The coordinate system used in the modelling of the SMSE/PVDF VEH

By taking into account the PM geometries, the magnetic field distribution along x, (B_x) and y, (B_y) of a rectangular PM is [28],

$$
\begin{cases}
B_x(x,y) = k_{pm}\left[\begin{array}{l} -\Psi\left(h_{pm}-y,\dfrac{w_{pm}}{2},x\right)-\Psi\left(y,\dfrac{w_{pm}}{2},x\right)-\Psi\left(\dfrac{w_{pm}}{2},h_{pm}-y,x\right)-\Psi\left(\dfrac{w_{pm}}{2},h_{pm}-y,x\right) \\[2mm] -\Psi\left(h_{pm}-y,\dfrac{w_{pm}}{2},x\right)-\Psi\left(y,\dfrac{w_{pm}}{2},x\right)-\Psi\left(\dfrac{w_{pm}}{2},y,x\right)-\Psi\left(\dfrac{w_{pm}}{2},y,x\right) \end{array}\right] \\[8mm]
B_y(x,y) = \dfrac{k_{pm}}{2}\left[-\Gamma\left(h_{pm}-y,\dfrac{w_{pm}}{2},x\right)-\Gamma\left(h_{pm}-y,x,\dfrac{w_{pm}}{2}\right)+\Gamma\left(y,\dfrac{w_{pm}}{2},x\right)+\Gamma\left(y,\dfrac{w_{pm}}{2},x\right)\right]
\end{cases}
\tag{1}
$$

where, h_{pm} and w_{pm} denote the height and width of the PM. k_{pm} is the field intensity parameter of the PM. In Eq. (1), Γ and Ψ are auxiliary functions that take the following form,

$$
\begin{cases}
\Gamma(\gamma_1,\gamma_2,\gamma_3) = \ln\dfrac{\sqrt{\gamma_1^2+\gamma_2^2+(\gamma_3-t_{pm})^2}-\gamma_2}{\sqrt{\gamma_1^2+\gamma_2^2+(\gamma_3-t_{pm})^2}+\gamma_2} - \ln\dfrac{\sqrt{\gamma_1^2+\gamma_2^2+\gamma_3^2}-\gamma_2}{\sqrt{\gamma_1^2+\gamma_2^2+\gamma_3^2}+\gamma_2} \\[4mm]
\Psi(\psi_1,\psi_2,\psi_3) = \tan^{-1}\left[\dfrac{\psi_1}{\psi_2}\dfrac{\psi_3-t_{pm}}{\sqrt{\psi_1^2+\psi_2^2+(\psi_3-t_{pm})^2}}\right] - \tan^{-1}\left[\dfrac{\psi_1}{\psi_2}\dfrac{\psi_3}{\sqrt{\psi_1^2+\psi_2^2+\psi_3^2}}\right]
\end{cases}
\tag{2}
$$

where, the independent variables of Γ and Ψ are $\gamma_1 \sim \gamma_3$ and $\psi_1 \sim \psi_3$ and t_{pm} denotes the thickness of the PM.

3.2 Energy and Work

Work by Magnetic Force

Treating the SMSE as a kind of flexible ferromagnetic material, the magnetic force distribution in x (f_{magx}) and y-direction (f_{magy}) are as in Eq. (3) respectively,

$$
\begin{cases}
f_{magx}(x,w) = A_{SMSE}\varphi_p\dfrac{\chi_x}{\mu_0}B_x(x,w)\dfrac{\partial B_x(x,w)}{\partial x} \\[4mm]
f_{magy}(x,w) = A_{SMSE}\varphi_p\dfrac{\chi_y}{\mu_0}B_y(x,w)\dfrac{\partial B_y(x,w)}{\partial x}
\end{cases}
\tag{3}
$$

where, w denotes the displacement relative to the base in the y-direction; A_{SMSE} is the cross-sectional area of the SMSE substrate; φ_p is the mass ratio of iron particles to the whole mixture in the SMSE substrate; χ_x and χ_y are the equivalent magnetic susceptibilities of the cantilever in the x- and y-directions, respectively.

From Eq. (3), the magnetic work in horizontal (W_{magx}) and vertical (W_{magy}) directions are represented as

6

$$\begin{cases} W_{magx} = \dfrac{1}{2}\int_0^l F_{magx}\left(x,w\right)\left(\dfrac{\partial w}{\partial x}\right)^2 \mathrm{d}x \\ W_{magy} = \int_0^l f_{magy}w\mathrm{d}x = \int_0^l\left[k_{magy}w + \Pi\left(x,w\right)\right]w\mathrm{d}x \end{cases} \tag{4}$$

in which, the magnetic force density along the y-direction f_{magy} comprises the linear component $k_{magy}w$ and nonlinear component $\Pi\left(x,w\right)$. l is the length of SMSE/PVDF cantilever, F_{magx} denotes the magnetic force at the position of x along the cantilever and can be expressed as,

$$F_{magx}\left(x,w\right) = \int_x^l f_{magx}\left(x,w\right)\mathrm{d}x \tag{5}$$

Strain Energy

The constitutive equations of the piezoelectric material follow a linear relation [29],

$$\begin{cases} D = \varepsilon_{33}E + d_{31}\sigma \\ \sigma = Y_p\left(s - d_{31}E\right) \end{cases} \tag{6}$$

where, D and E are the electric displacements and electric field intensity of the PVDF layer. σ and s are the stress and strain of the piezoelectric material; Y_p is Young's modulus of the piezoelectric material. ε_{33} is the dielectric coefficient and d_{31} the piezoelectric coefficient.

For the PVDF layer, the electrical field intensity is

$$E = \frac{V}{h_p} \tag{7}$$

where V is the voltage across the PVDF layer and h_p is its thickness. When the deflection is small, we assume the cantilever as a Euler-Bernoulli beam. Its strain energy of a the could be written as

$$U_{strain} = \frac{1}{2}\int_0^l YI\left(\frac{\partial^2 w}{\partial x^2}\right)^2 \mathrm{d}x - \frac{1}{2}\int_0^l \vartheta V\left(\frac{\partial^2 w}{\partial x^2}\right)\mathrm{d}x \tag{8}$$

where YI is the bending stiffness of the composite cantilever and ϑ is the electromechanical coupling coefficient. Theoretically, YI is determined via the Young's modulus, thickness and width of each layer in the composite cantilever [29]; ϑ could be calculated via Young's modulus, piezoelectric constant, thickness and width of the PVDF layer, as well as the distance between

PVDF layer to the neutral plane of the composite cantilever [30]. However, the theoretical methods cannot be utilized directly to determine YI and ϑ in our SMSE/PVDF composite cantilever. This is because the PVDF is a sandwich structure. There are two thin electrode layers sandwiching the piezoelectric polymer layer. The thicknesses of electrodes on top and bottom surfaces of the PVDF layer cannot be guaranteed to be uniform and are very difficult to quantify. The thickness of the PVDF layer itself is not perfectly uniform. Moreover, in the fabrication procedure of the SMSE layer, we cannot guarantee an ideally homogenous distribution of the iron particles in the Eco-flex matrix. As a result, the thickness and Young's modulus in PVDF and SMSE layers are not uniform. The neutral plane position of the cantilever is also uncertain. For ease of numerical modelling, we neglect the above uncertainties and use parameter identification method to determine the overall bending stiffness and the electromechanical coupling coefficient of the SMSE/PVDF composite cantilever in Eq. (8). The identification procedure will be detailed in Section 4.2.

Electrical Potential Energy and Work by Electrical Force

The electrical potential energy takes the following form,

$$U_E = \frac{1}{2}\int_0^l \int_{h_b}^{h_c} b \frac{V}{h_p}\left(d_{31} y \frac{\partial^2 w}{\partial x^2} + \varepsilon_{33}\frac{V}{h_2} \right) \mathrm{d}y \mathrm{d}x = \frac{1}{2}\int_0^l \left(\vartheta V \frac{\partial^2 w}{\partial x^2} + C_p V^2 \right) \mathrm{d}x \qquad (9)$$

where,

$$C_p = \int_0^l \int_{h_b}^{h_c} \frac{\varepsilon_{33} b}{h_p^2}\mathrm{d}y\mathrm{d}x = \frac{\varepsilon_{33}bl}{h_p} \qquad (10)$$

During vibration, the amount of work from the electrical force to carry a certain amount of charge (Q) from one side to the other side of the PVDF layer is expressed as,

$$W_E = -\int_0^l VQ\mathrm{d}x \qquad (11)$$

Kinetic Energy and Work by Exciting Force

The kinetic energy (T) of the cantilever is,

$$T = \int_0^l \frac{\rho A_{cs}}{2}\left(\frac{\partial w}{\partial t} \right)^2 \mathrm{d}x \qquad (12)$$

where, ρ and A_{cs} are the density and cross-sectional area of the composite cantilever beam.

8

The total work from the exciting force (f_{ext}) is

$$W_{ext} = \int_0^l f_{ext} w \mathrm{d}x = \int_0^l \rho A_{cs} a_{cc} w \mathrm{d}x \tag{13}$$

where, a_{cc} is the acceleration of the base excitation.

3.3 Hamilton Principle and Governing Equation

The governing equation could be expressed using the extended Hamilton's principle,

$$\int_{t_1}^{t_2} \left(\delta T - \delta U_{strain} - \delta U_E + \delta W_{magy} + \delta W_{magx} + \delta W_E + \delta W_{ext} \right) \mathrm{d}t = 0, \ \ \delta w(x,t) = 0, \ \ 0 \le x \le l \ \ t = t_{1,2} \tag{14}$$

For this SMSE/PVDF-VEH, a continuous system expressed in Eq. (14) cannot be utilized directly. That is because the magnetic field distribution along the cantilever is uneven. Horizontal magnetic force for different positions along the beam is different. Therefore, a discrete model is required to discretize the cantilever into multiple finite elements. In this paper, the finite element (FE) method is applied to discretize the system.

3.4 Finite Element Model

According to the finite element method, the displacement distribution in one element takes the following form,

$$w = \sum_{i=1}^4 u_{ei} N_i(\xi) \tag{15}$$

where u_{ei} (i=1,2,3,4) are the four nodal displacements (two translations and two rotations) in each finite element; ξ is the local coordinate of one certain element. $N_i(\xi)$ (i=1,2,3,4) is the shape functions, which could be referred to [31]. In this paper, voltage in each finite element is assumed to be constant and regarded as another degree of freedom. In addition, the magnetic field distribution in each finite element is treated as constant.

As the energy expression does not change its form with the coordinate system, Eq. (15) could be substituted directly into the energy and work expressions in Eq. (4), Eq. (8), Eq. (9), Eq. (11), Eq. (12), Eq. (13) to obtain the energy and work expressions in each element.

Furthermore, the variation form of the strain energy in one element is,

9

$$\delta U_{strain} = \int_0^{l_e} YI \sum_{i,j} \frac{\mathrm{d}^2 N_i}{\mathrm{d}\xi^2} \frac{\mathrm{d}^2 N_j}{\mathrm{d}\xi^2} u_{ei} \delta u_{ei} \mathrm{d}\xi - \int_0^{l_e} \frac{1}{2} \vartheta \sum_i \frac{\mathrm{d}^2 N_i}{\mathrm{d}\xi^2} u_{ei} \delta V \mathrm{d}\xi - \int_0^{l_e} \frac{1}{2} \vartheta V \sum_i \frac{\mathrm{d}^2 N_i}{\mathrm{d}\xi^2} \delta u_{ei} \mathrm{d}\xi \quad (16)$$

where, l_e is the length of the element. The beam is meshed uniformly and thus

$$l_e = \frac{l}{n} \qquad (17)$$

where, n is the number of the element.

The variation of U_E in each element is expressed as

$$\delta U_E = \delta \left(\int_0^{l_e} \frac{1}{2} \vartheta V \frac{\partial^2 w}{\partial \xi^2} \mathrm{d}\xi \right) + \delta \left(\int_0^{l_e} \frac{1}{2} \frac{C_p}{n} V^2 \mathrm{d}\xi \right) = \int_0^{l_e} \frac{1}{2} \vartheta \sum_i \frac{\mathrm{d}^2 N_i}{\mathrm{d}\xi^2} u_{ei} \delta V \mathrm{d}\xi + \int_0^{l_e} \frac{C_p}{n} V \delta V \mathrm{d}\xi \quad (18)$$

The variation of W_E is

$$\delta W_E = -\int_0^{l_e} Q_e \delta V \mathrm{d}\xi \qquad (19)$$

where, Q_e is the charge generated by one element. In each element, the governing equation expressed using shape functions is

$$\int_0^{l_e} \left(\begin{array}{l} YI \sum_{i,j} \frac{\mathrm{d}^2 N_i}{\mathrm{d}\xi^2} \frac{\mathrm{d}^2 N_j}{\mathrm{d}\xi^2} u_{ei} \delta u_{ei} + F_{magx} \sum_{i,j} \frac{\mathrm{d}N_i}{\mathrm{d}\xi} \frac{\mathrm{d}N_j}{\mathrm{d}\xi} u_{ei} \delta u_{ei} - \rho A_{cs} \sum_{i,j} N_i N_j \ddot{u}_{ei} \delta u_{ei} \\ -k_{magy} \sum_{i,j} N_i N_j u_{ei} \delta u_{ei} - \left[f_{ext} + \Pi \right] \sum_j N_j \delta u_{ei} \\ -\vartheta \sum_i \frac{\mathrm{d}^2 N_i}{\mathrm{d}\xi^2} u_{ei} \delta V - \vartheta \sum_i \frac{\mathrm{d}^2 N_i}{\mathrm{d}\xi^2} V \delta u_{ei} - \frac{C_p}{n} V \delta V - q_e \delta V \end{array} \right) \mathrm{d}\xi$$

$$= \int_0^{l_e} \left[\begin{array}{l} \left(YI \sum_{i,j} \frac{\mathrm{d}^2 N_i}{\mathrm{d}\xi^2} \frac{\mathrm{d}^2 N_j}{\mathrm{d}\xi^2} u_{ei} + F_{magx} \sum_{i,j} \frac{\mathrm{d}N_i}{\mathrm{d}\xi} \frac{\mathrm{d}N_j}{\mathrm{d}\xi} u_{ei} - \rho A_{cs} \sum_{i,j} N_i N_j \ddot{u}_{ei} \\ -k_{magy} \sum_{i,j} N_i N_j u_{ei} - \left[f_{ext} + \Pi \right] \sum_j N_j - \vartheta \sum_i \frac{\mathrm{d}^2 N_i}{\mathrm{d}\xi^2} V \right) \delta u_{ei} \\ -\left(\vartheta \sum_i \frac{\mathrm{d}^2 N_i}{\mathrm{d}\xi^2} u_{ei} + \frac{C_p}{n} V + Q_e \right) \delta V \end{array} \right] \mathrm{d}\xi = 0$$

$$(20)$$

Eventually, the mass matrix $[M_e]$, stiffness matrix $[K_e]$, force vector $[F_{ye}]$ and the transforming vector $[T_e]$ are

$$
\begin{cases}
[M_e]_{ij} = \rho A_{cs} \displaystyle\int_0^{l_e} N_i N_j \mathrm{d}\xi \\[4mm]
[K_e]_{ij} = \displaystyle\int_0^{l_e} \left(YI \frac{\mathrm{d}^2 N_i}{\mathrm{d}\xi^2} \frac{\mathrm{d}^2 N_j}{\mathrm{d}\xi^2} + F_{magx} \frac{\mathrm{d}N_i}{\mathrm{d}\xi} \frac{\mathrm{d}N_j}{\mathrm{d}\xi} - k_{magy} N_i N_j \right) \mathrm{d}\xi \\[4mm]
[F_{ye}]_j = \displaystyle\int_0^{l_e} \Big[f_{ext} + \Pi\big(x_{e,k}, w\big) \Big] N_j \mathrm{d}\xi \\[4mm]
[T_e]_j = \displaystyle\int_0^{l_e} \vartheta \frac{\mathrm{d}^2 N_j}{\mathrm{d}\xi^2} \mathrm{d}\xi
\end{cases} \tag{21}
$$

in which, $[\ ]_{ij}$ denotes the entry at i^{th} row and j^{th} column in the matrix. The detailed expressions of element matrices in Eq. (21) are

$$
\begin{cases}
[K_e] = \dfrac{YI}{l_e^{\,3}}
\begin{bmatrix}
12 & 6l_e & -12 & 6l_e \\
6l_e & 4l_e^{\,2} & -6l_e & 2l_e^{\,2} \\
-12 & -6l_e & 12 & -6l_e \\
6l_e & 2l_e^{\,2} & -6l_e & 4l_e^{\,2}
\end{bmatrix}
+ \dfrac{F_{magx}}{30 l_e}
\begin{bmatrix}
36 & 3l_e & -36 & 3l_e \\
3l_e & 6l_e^{\,2} & -3l_e & -l_e^{\,2} \\
-36 & -3l_e & 36 & -3l_e \\
3l_e & -l_e^{\,2} & -3l_e & 4l_e^{\,2}
\end{bmatrix} \\[12mm]
\qquad - \dfrac{k_{magy} l_e}{420}
\begin{bmatrix}
156 & 22l_e & 54 & -13l_e \\
22l_e & 4l_e^{\,2} & 13l_e & -3l_e^{\,2} \\
54 & 13l_e & 156 & -22l_e \\
-13l_e & -3l_e^{\,2} & -22l_e & 4l_e^{\,2}
\end{bmatrix} \\[12mm]
\qquad\qquad [M_e] = \dfrac{\rho A_{cs} l_e}{420}
\begin{bmatrix}
156 & 22l_e & 54 & -13l_e \\
22l_e & 4l_e^{\,2} & 13l_e & -3l_e^{\,2} \\
54 & 13l_e & 156 & -22l_e \\
-13l_e & -3l_e^{\,2} & -22l_e & 4l_e^{\,2}
\end{bmatrix} \\[12mm]
\qquad\qquad [F_{ye}] = \big(f_{ext} + \Pi(x_{e,k}, w)\big) \dfrac{l_e}{2} \begin{bmatrix} 1 & 6l_e & 1 & -6l_e \end{bmatrix}^T \\[4mm]
\qquad\qquad\qquad [T_e] = \vartheta \begin{bmatrix} 0 & -1 & 0 & 1 \end{bmatrix}^T
\end{cases} \tag{22}
$$

Assembling the element matrices and vectors in Eq. (22), the governing equation of the discretized SMSE/PVDF cantilever could be expressed as,

$$
\begin{cases}
[M][\ddot{u}] + [C][\dot{u}] + [K][u] - [T][V] = [F_y] \\[3mm]
\dfrac{C_p}{n}[V] + [Q_e] + [T]^T[u] = 0
\end{cases} \tag{23}
$$

where $[M]$, $[C]$, $[K]$ are global mass, damping and stiffness matrices; $[Q_e]$ is the vector composed of charges in each element; $[T]$ is the global transforming matrix, taking the following form,

11

$$
T = \begin{bmatrix}
0 & 0 & 0 & 0 & \cdots & 0 \\
\vartheta & -\vartheta & 0 & 0 & \cdots & 0 \\
0 & 0 & 0 & 0 & \cdots & 0 \\
0 & \vartheta & -\vartheta & 0 & \cdots & 0 \\
0 & 0 & 0 & 0 & \cdots & 0 \\
0 & 0 & \vartheta & \vartheta & \cdots & 0 \\
0 & 0 & 0 & 0 & \cdots & 0 \\
0 & 0 & 0 & -\vartheta & \cdots & \cdots \\
0 & 0 & 0 & 0 & \cdots & 0 \\
0 & 0 & 0 & 0 & \cdots & -\vartheta \\
\vdots & \vdots & \vdots & \vdots & \cdots & 0 \\
0 & 0 & 0 & 0 & \cdots & \vartheta
\end{bmatrix}_{2n \times 2n}
\tag{24}
$$

Note that the PVDF layer has electrodes on both sides, which means the voltage (V_e) and charge (q_e) is constant along the whole beam. i.e.

$$
V_{e1} = V_{e2} = \cdots = V_{en} = V_e \Rightarrow [V] = V_e[1 \quad 1 \quad \cdots \quad 1]^T
\tag{25}
$$

Substituting Eq. (25) into Eq. (23) and differentiate the second equation in Eq. (23) with respect to time, the governing equation is deduced as,

$$
\begin{cases}
[M][\ddot{u}] + [C][\dot{u}] + [K][u] - [\tilde{T}]V_e = [F] \\
C_p\dot{V}_e + \dot{Q} + [\tilde{T}]^T[\dot{u}] = 0
\end{cases}
\tag{26}
$$

where $[\tilde{T}] = [T][1 \quad 1 \quad \cdots \quad 1]^T$, R_L denotes the load resistance.

3.5 Model Reduction

In order to properly describe the unevenness of the magnetic field in *x*-direction, 20 elements are selected for the FE model (*n*=20). Therefore, the matrix dimensions in Eq. (26) reach up 40×40 after the boundary conditions are enforced (i.e., removing the first two rows and two columns in the [*M*] and [*K*]). Given the nonlinearity in the system, further mathematical treatments have to be taken to reduce the computing cost.

When the vibration amplitude is low, the system could be regarded as a linear system with a fixed stiffness matrix [*K*(0)]. The corresponding modal matrix could be obtained after solving the algebraic eigenvalue problem in Eq. (27),

12

$$[K(0)][\varphi_i] = \omega_i^2 [M][\varphi_i] \tag{27}$$

Here ω_i denotes i^{th} mode. φ_i denotes the ith modal vector. The linear system could be decoupled using the modal matrix formed by the modal vectors.

When the cantilever vibrates with large amplitude, the mass matrix $[M]$ is unchanged but the stiffness matrix will vary with time and the nonlinearity is involved. Theoretically, the modal matrix also changes accordingly with the varying stiffness matrix. However, evidenced by the simulation and experimental results, there is no obvious change between the linear modal shape and the nonlinear varying mode shape. Therefore, the first three vectors will be selected as the 'assumed modes', i.e. $[\Phi] = \left[[\varphi_1], [\varphi_2], [\varphi_3] \right]$ of the discretized nonlinear system and kept unchanged.

With the help of $[\Phi]$, the original finite element model could be reduced to a much more computable version with reduced matrices (3×3) and vectors as follows:

$$\begin{cases} [M_{rd}] = [\Phi]^T [M][\Phi] \\ [K_{rd}(t)] = [\Phi]^T [K(t)][\Phi] \\ [F_{rd}(t)] = [\Phi]^T [F(t)] \\ [u_{rd}(t)] = [\Phi]^T [u(t)] \\ \left[E_{rd}(t) \right] = [\Phi]^T [\tilde{T}] V_e \end{cases} \tag{28}$$

where, $[M_{rd}]$, $[K_{rd}(t)]$, $[F_{rd}(t)]$, $[u_{rd}(t)]$ and $\left[E_{rd}(t) \right]$ are the reduced mass matrix, stiffness matrix, force vector, displacement vector and electrical field force vector in the modal space. The mass matrix $[M]$ is unchanged and thus still diagonalizable. Except for the mass matrix, all other matrices/vectors are time-dependent.

The damping ratio ς identified from the impulse test is the first modal damping ratio. Here it is assumed that the modal damping ratios for higher order modes equal to the first one. As a result, the reduced damping matrix could be expressed as,

$$[C_{rd}] = Diag\left(\begin{array}{ccc} 2\varsigma\sqrt{[M_{rd}]_{1,1}[K_{rd}(t)]_{1,1}} & 2\varsigma\sqrt{[M_{rd}]_{2,2}[K_{rd}(t)]_{2,2}} & 2\varsigma\sqrt{[M_{rd}]_{3,3}[K_{rd}(t)]_{3,3}} \end{array} \right) \tag{29}$$

where, $Diag([\ ])$ represents a diagonal matrix.

13

Since $[M_{rd}]$ is diagonalized, the first equation of Eq. (26) can be transformed into the state-space form and solved with the Runge-Kutta method as follows.

$$\begin{pmatrix} [\dot{u}_{rd}] \\ [\ddot{u}_{rd}] \end{pmatrix} = \begin{pmatrix} 0 & Diag([1,1,1]) \\ -M_{rd}^{-1}K_{rd}(t) & -M_{rd}^{-1}C_{rd} \end{pmatrix} \begin{pmatrix} [u_{rd}] \\ [\dot{u}_{rd}] \end{pmatrix} + \begin{pmatrix} 0 \\ M_{rd}^{-1}[F_{rd}(t) + E_{rd}(t)] \end{pmatrix} \quad (30)$$

The parameters for the simulation are listed in Table 1.

Table 1. System Parameters

Parameter	Value
Piezoelectric coefficient, d_{31}	23 pC/N
Relative dielectric coefficient, ε_{33}	12
Dielectric coefficient of vacuum, ε_0	8.854×10^{-12} F/m
Height of PM, h_{pm}	9 mm
Width of PM, w_{pm}	25 mm
Thickness of PM, t_{pm}	3 mm
Field intensity parameter, k_{pm}	0.101
Width of SMSE/PVDF cantilever, b	15 mm
Length of SMSE/PVDF cantilever, l	46 mm
Mass of SMSE/PVDF cantilever, m	3.7 g (Prototype 1); 5.68 g (Prototype 2)
Thickness of PVDF layer, h_p	0.1 mm

4. Experimental Setup and Parameter Identification

4.1 Experiment setup

The vibration testing system is shown in Figure 4, composed of a dynamic controller (VR9500, Vibration Research Corp.), a power amplifier (APS125, APS Dynamics Corp.) to intensify the controlling signal from the controller, a shaker (APS113, APS Dynamics Corp.) to convert the electrical signal into mechanical vibration and an accelerometer (352A56, PCB Piezotronics Inc.) to measure the acceleration as feedback to the controller. Two laser displacement sensors (CP08MHT80, Wenglor Corp.) were used to measure the displacement at the middle of the SMSE cantilever and the base displacement, respectively. We recorded the middle position displacement because the tip displacement of SMSE/PVDF cantilever has exceeded the measurement range of the laser sensors. The relative displacement is obtained as the difference between the middle position displacement and the base displacement. A data acquisition card NI 9215 (National Instrument) was used to pick up the signals from laser sensors; while the voltage generated by the PVDF was acquired by another card NI 9205 (National Instrument).

14

NI 9205 was used to read the output voltage from the PVDF as it has a very large input impendence (over10 GΩ) to match the internal impendence of the PVDF.
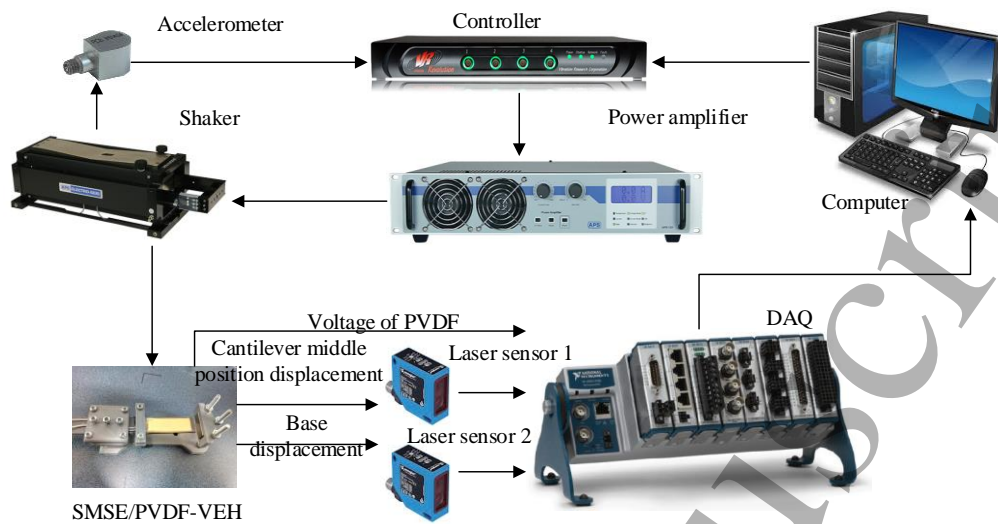

Figure 4. Vibration testing setup

4.2 Parameter Identification

Before simulation, some parameters of the SMSE/PVDF cantilever have to be determined experimentally such as bending stiffness of PVDF/SMSE cantilever (*YI*), damping ratio of PVDF/SME cantilever (ς), linear damped natural frequency of PVDF/SMSE cantilever with and without PM (f_{d1}, f_{d0}), horizontal and vertical equivalent magnetic susceptibility of SMSE layer (χ_x, χ_y), and finally the electromechanical coupling coefficient of the PVDF layer (ϑ). Parameter identification is based on an impulse test and static magnetic force test. The procedure for parameter identification is shown in Figure 5.
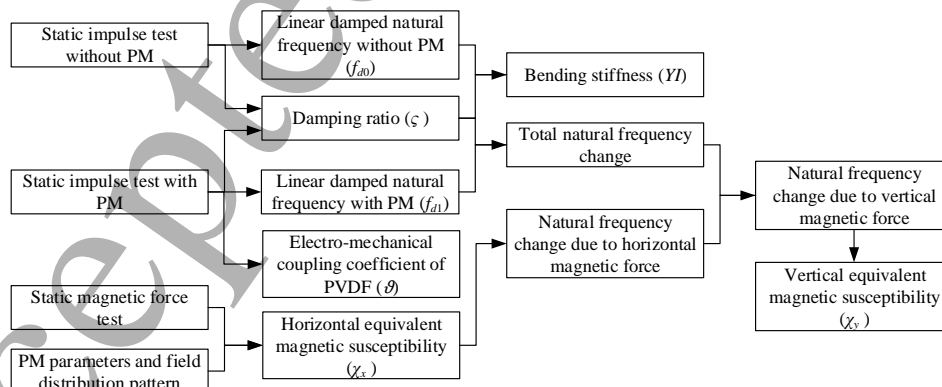

Figure 5. Parameter identification process

The linear damped natural frequency (f_d) can be determined by an impulse test. The damping ratio ς can also be determined from the impulse test using the logarithmic decrement method.

15

Then the linear natural frequency (f_n) is determined using f_d and ς. The bending stiffness (YI) can then be estimated using the linear natural frequency of the cantilever. The impulse should be very small to make sure we can get a quasi-linear response from the cantilever.

The equivalent magnetic susceptibility in the x-direction (χ_x) is determined by measuring the initial tension of the cantilever, $F_T(0,0)$, using a force sensor (Precision Digital Force Gauge FGD-50), where , χ_x could be expressed as

$$\chi_x = \frac{F_T(0,0)}{\sum_{k=1}^{n}\left(\frac{A_{cs}\varphi_p l_e}{\mu_0} B_x\left(x_{e,k},0\right)\frac{\partial B_x\left(x_{e,k},0\right)}{\partial x}\right)} \tag{31}$$

The equivalent magnetic susceptibility in the y-direction (χ_y) could be determined by its contribution through the change in the cantilever's stiffness. As we believe the change in the linear stiffness of the cantilever comes solely from two parts; i.e., the tension increase due to the horizontal magnetic force and the linear component of the vertical magnetic force. As the total change of stiffness and the stiffness change after the horizontal component of magnetic force is known, the numerical value of the linear part of the vertical magnetic force can be determined. χ_y could then be determined.

The electromechanical coupling coefficient (ϑ) could be determined from the open circuit voltage V_{open} and tip displacement response of the cantilever from the impulse test. According to Eq. (24)

$$\left[\tilde{T}\right] = [T][1 \quad 1 \quad \cdots \quad 1]^T = [0\cdots 0, \vartheta] \tag{32}$$

In the open circuit condition, the second equation in Eq. (26) takes the following form,

$$C_p V_{open} = \left[\tilde{T}\right]^T [u] = \vartheta \frac{\partial w_{tip}}{\partial x} \tag{33}$$

Integrating with respect to x on both sides, yields

$$\int_0^l C_p V_{open}\mathrm{d}x = \vartheta w_{tip} \tag{34}$$

As the voltage is independent of the horizontal coordinate, the identification expression for ϑ can be deduced from Eq. (34),

$$\vartheta = \frac{C_p V_{open} l}{w_{tip}} \tag{35}$$

16

Practically, w_{tip} and V_{open} is obtained by extracting the tip displacement and voltage peaks of the SMSE/PVDF cantilever from the impulse tests, which are shown as Figure 6. With the cantilever-PM gap of 5 mm, the parameter identification results for both prototypes are summarised as Table 2.
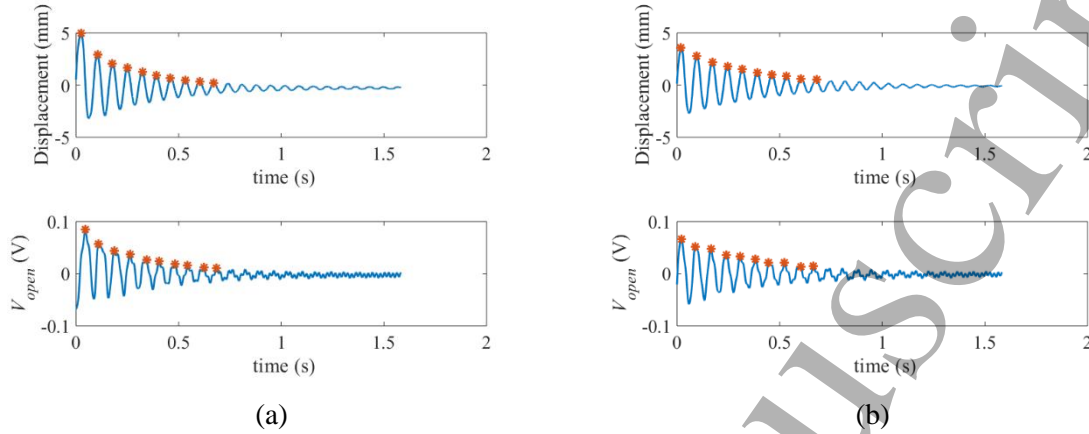

(a)   (b)

Figure 6. Impulse test results for the SMSE/PVDF cantilever: (a) Prototype 1; (b) Prototype 2

Table 2. Parameter identification results

Parameter	Prototype 1	Prototype 2
Linear damped natural frequency without PM (f_{d0})	4.32 Hz	6.89 Hz
Linear damped natural frequency with PM (f_{d1})	13.94 Hz	13.45 Hz
Damping ratio (ζ)	0.032	0.037
Bending stiffness (YI)	1.98×10^{-5} Nm^2	6.47×10^{-5} Nm^2
Static magnetic force in ($F_T(0,0)$)	0.055 N	0.060 N
Equivalent magnetic susceptibility in x direction (χ_x)	1.49	1.06
Equivalent magnetic susceptibility in x direction (χ_y)	6.89	6.78
Electromechanical coupling coefficient (ϑ)	2.22×10^{-9}	2.18×10^{-9}

5. Results and Discussion

5.1 Frequency Bandwidth Broadening Analysis

The simulated and measured frequency responses of the SMSE/PVDF-VEH prototypes are shown in Figure 7 and Figure 8. As mentioned in Section 4.1, the middle point displacement was measured since the free end deflection exceeded measurement range of the laser sensor. Accordingly, for the simulation results, we calculate the displacement of the element in the middle position of the cantilever for fair comparison with the experimental measurement at the same position.
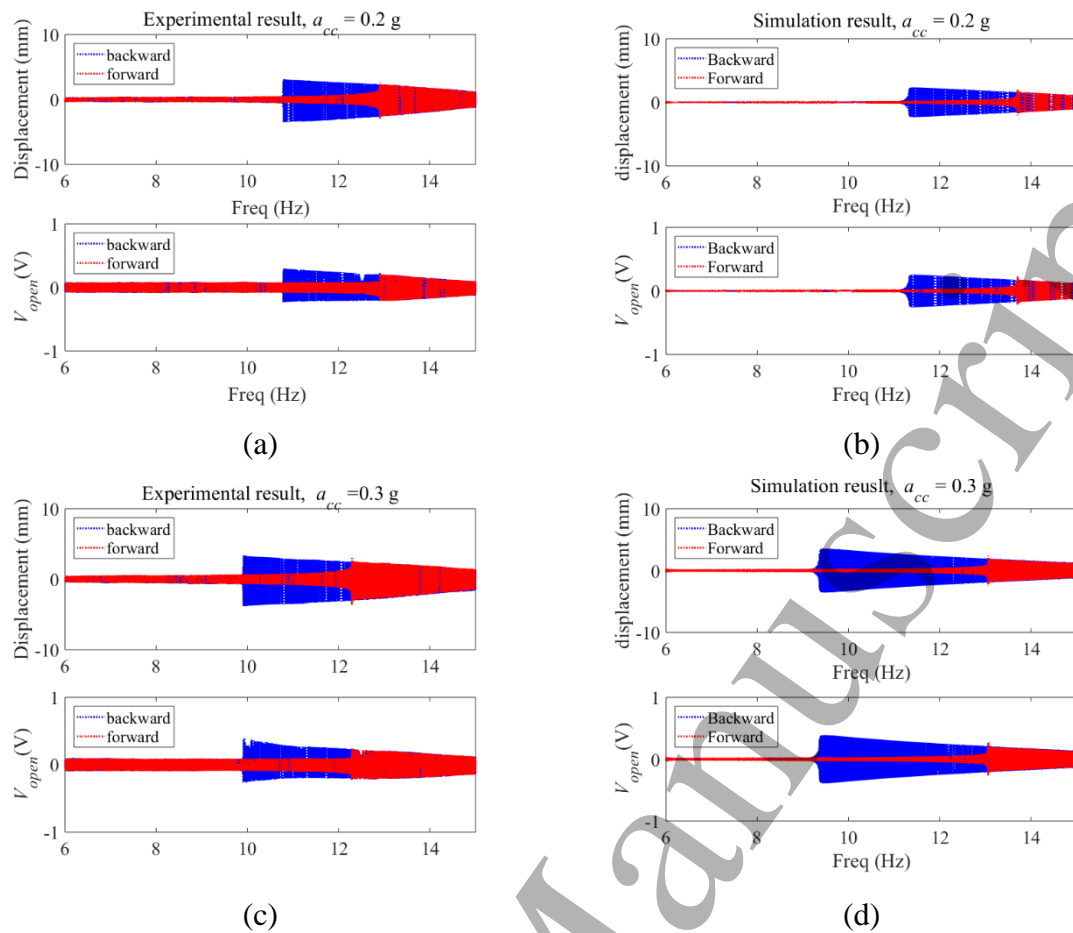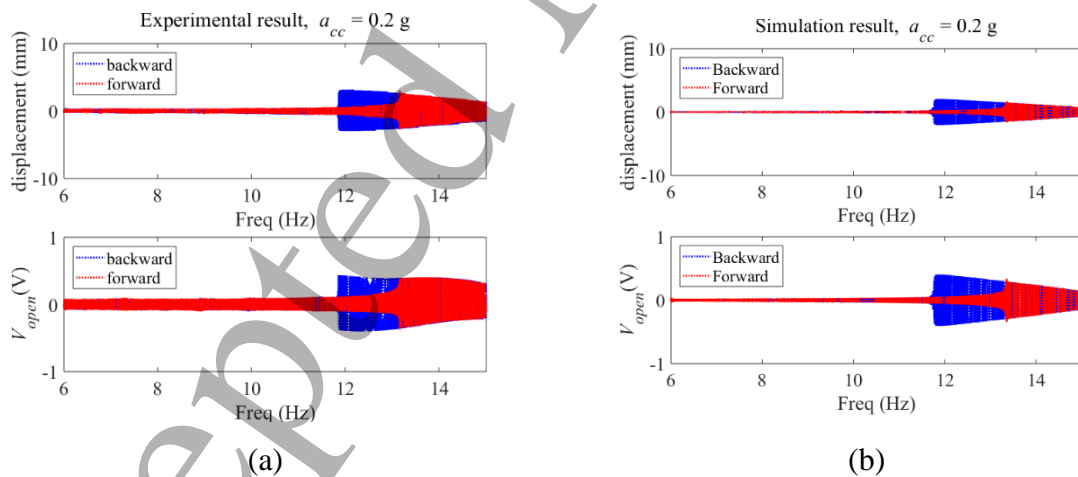
17

Figure 7. Simulated and measured frequency responses of Prototype 1 (SMSE layer thickness = 3 mm)
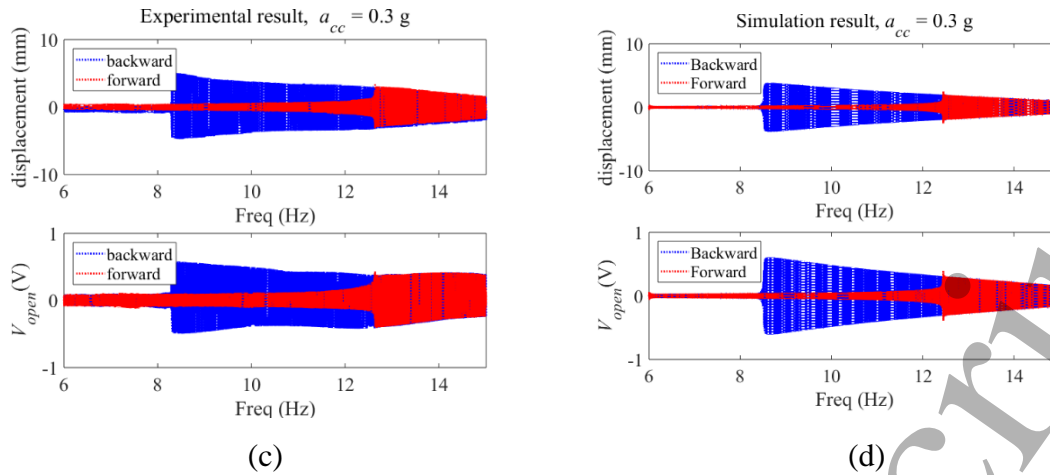
Figure 8. Simulated and measured frequency responses of Prototype 2 (SMSE layer thickness = 5 mm)

As shown in Figure 7 and Figure 8, with the help of a PM and the induced nonlinear softening effect, the frequency bandwidth of an SMSE/PVDF cantilever has been considerably widened. In general, the simulated frequency responses qualitatively agree with the experimental measurements in terms of the voltage magnitude and the frequency range.

There are a few possible reasons responsible for the discrepancies between the simulation and experimental results. As for the displacement results, one possible reason for the discrepancies is that we do not consider the geometrical nonlinearity in the beam bending model. When the deflection of the SMSE/PVDF cantilever is large, it cannot be ideally described by the Euler-Bernoulli beam model in Eq.(8). As a result, the calculated displacement is slightly different from the experimental results. As for the voltage results, the electromechanical coefficient (ϑ) is regarded as an unchanged constant in all the elements. However, due to the inevitable unevenness in PVDF thickness and the inhomogeneity in the SMSE material, the practical position of the neutral plane varies in different elements. As a result, the practical ϑ changes its value in different elements.

There is a slight non-uniformity in the experimental voltage results. One possible reason for this non-uniformity is the hysteresis of the piezoelectric material [32], which is not considered in the modelling. Due to this hysteresis property, the peak-to-peak voltage does not vary uniformly during the frequency sweep.

It should be noted in Figure 7 and 8 that there are two orbits in the multi-solution range between backward and forward jumping frequencies. In a practical environment with unknown initial conditions, the harvester may vibrate in either orbit. Nevertheless, the broadband performance

19

could be realized only if the harvester captures and maintains the high energy orbit. Once the harvester is attracted to the low energy orbit, it will not be efficient for power generation. Therefore, the basin of attraction of such nonlinear harvester is useful [33]. However, it is difficult to perform such an analysis in this study because our model cannot be described as a simple Duffing equation and it has multiple degrees of freedom.

5.2 'Force Valley' Effect

SMSE is a highly magneto-sensitive material. Apart from the gap between the SMSE/PVDF cantilever and the PM, the dynamic behavior of the cantilever can even be altered by the magnetic field distribution of the PM. Specifically, if we vibrate the SMSE/PVDF cantilever near a rectangular PM, an interesting 'force valley' effect could be observed. This effect is further explained in the following paragraphs.

Two PMs with different dimensions are selected: width/ height/ thickness = 25 mm/9 mm/ 3mm for the PM1; width/ height/ thickness = 25 mm /25 mm/ 5 mm for the PM2. A picture for PM1 and PM2 are shown in Figure 9.

Figure 9. PM1 and PM2

As shown in Figure 1 (b) and (c), the magnetization direction of the rectangular PM is along the horizontal direction of the cantilever. The change in the horizontal component of the magnetic force density (f_{magx}) will predominate the change of the nonlinear stiffness of the SMSE/PVDF cantilever during vibration. As a result, we can use the spatial distribution of the f_{magx} to indicate the change of the stiffness of the cantilever during vibration.

The horizontal magnetic force density of SMSE/PVDF-VEH at different spatial positions is shown in Figure 10. The coordinate system is shown as Figure 10 (a). The origin is selected as the geometric center of PM, y_1 is the same as y in Figure 3; x_1 is opposite to x, pointing away from the PM towards the cantilever.

20

According to Eq. (3), the horizontal magnetic force distribution for the different spatial position is calculated. The results are shown in Figure 10 (b) and (c). In order to highlight the distribution pattern, the magnetic force distribution is normalized as $\hat{f}_{magx}$.
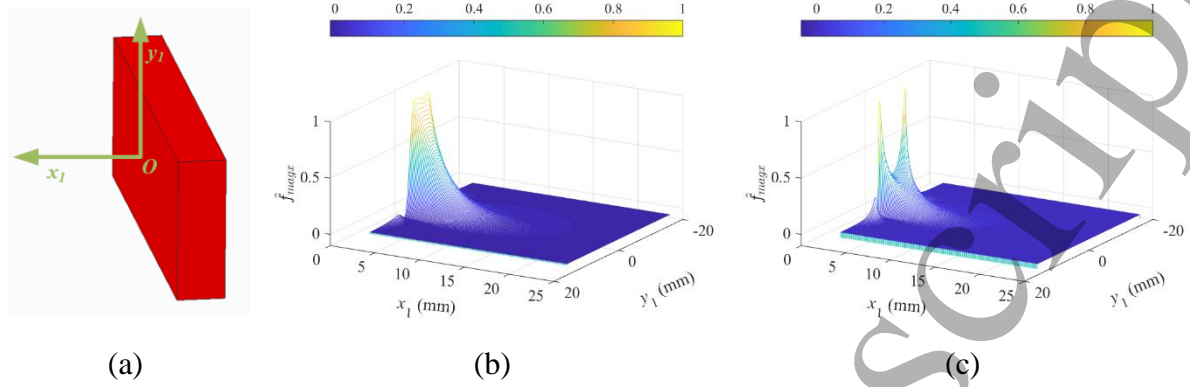

(a)   (b)   (c)

Figure 10. Normalized horizontal magnetic force density distribution: (a) Coordinate system; (b) Normalized horizontal magnetic force distribution with PM1; (c) Normalized horizontal magnetic force distribution with PM2;

Figure 10 (b) and (c) show that in general, the magnetic force decreases away from the origin in both x_1 and y_1 directions. Interestingly, in Figure 10 (c), there are two peaks when the cantilever-PM gap is small. The two peaks are due to the flux streamlines get denser near the upper and lower edges of the PM, which lead to a larger flux density ($\vec{B}$) as well as the steeper gradient along x_1 direction ($\partial \vec{B}/\partial x_1$). As a result, there is a valley between the two peaks, as shown in Figure 11. Within this valley, the magnetic force density increases from the equilibrium point. This region is termed as 'force valley'.
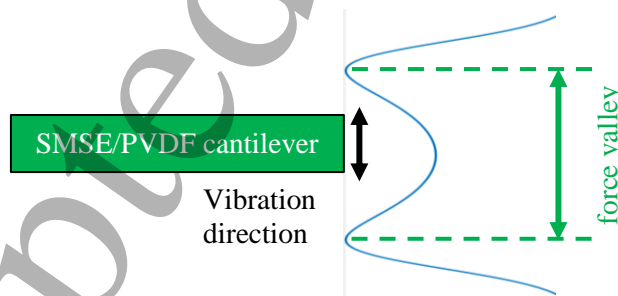

Figure 11. 'Force valley' in normalized horizontal magnetic force distribution at a certain cantilever-PM gap

As shown in Figure 11, the cantilever vibrates in y_1 direction. Due to the 'force valley', the stiffness of the system increases from the equilibrium point, leading to a hardening nonlinearity within the range of 'force valley'. Nevertheless, when the vibration amplitude of the free end

21

gets larger than the width of this 'force valley', the magnetic force drops and the cantilever will experience an overall softening nonlinearity effect.

As indicated in Figure 10, a more obvious 'force valley' happens with a rectangular PM with larger height and smaller cantilever-PM gap distance. In order to observe the changing pattern of the 'force valley' effect, we vibrate Prototype 1 in the magnetic field by PM2. The experimentally measured frequency responses for different cantilever-PM gap distances are shown in Figure 12.
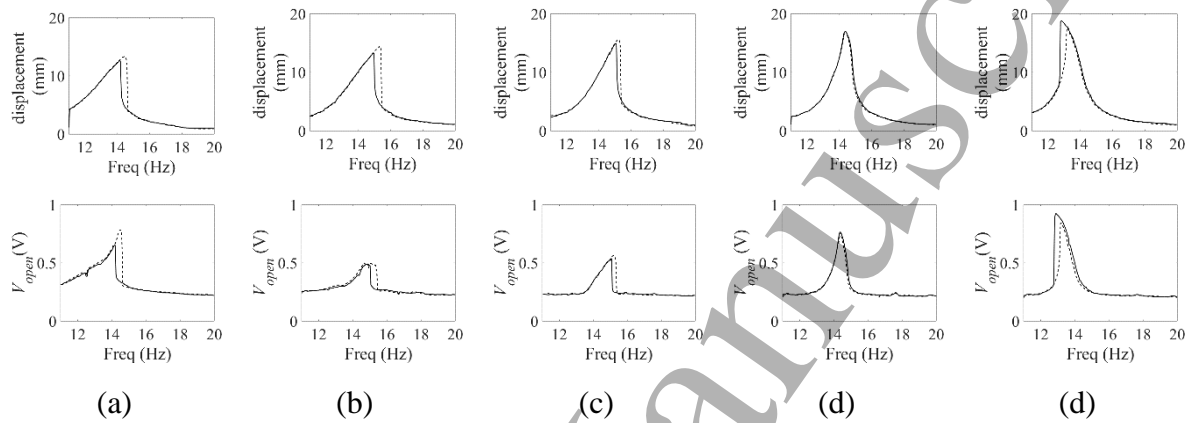

Figure 12. Measured frequency responses of a SMSE/PVDF-VEH porotype with different cantilever-PM gaps: (a) 2 mm; (b) 3 mm; (c) 4 mm; (d) 5 mm; (e) 6 mm. (dashed line for forward sweeping, solid line for backward sweeping)

As shown in Figure 12, the hardening nonlinearity is observed when the cantilever-PM gap is small. As the cantilever-PM gap increases, the hardening nonlinearity disappears and is replaced by the softening nonlinearity. Since the nonlinearity is related to the 'force valley', this observation could be explained with Figure 10 (c). With the increase of the cantilever-PM gap in x_1 direction, the width and depth of 'force valley' decrease and finally the 'force valley' disappears.

5.3 Power Output

The power generated at an acceleration level of 0.3 g for the two SMSE/PVDF-VEH prototypes with different load resistances can be calculated using the equation

$$P = \frac{V_{RMS}^2}{R_L} \tag{36}$$

22

where P is the average power generated on the load resistance, V_{RMS} is the peak to peak voltage of load resistance R_L divided by $\sqrt{2}$. The plotted power with different load resistances are shown in Figure 13.
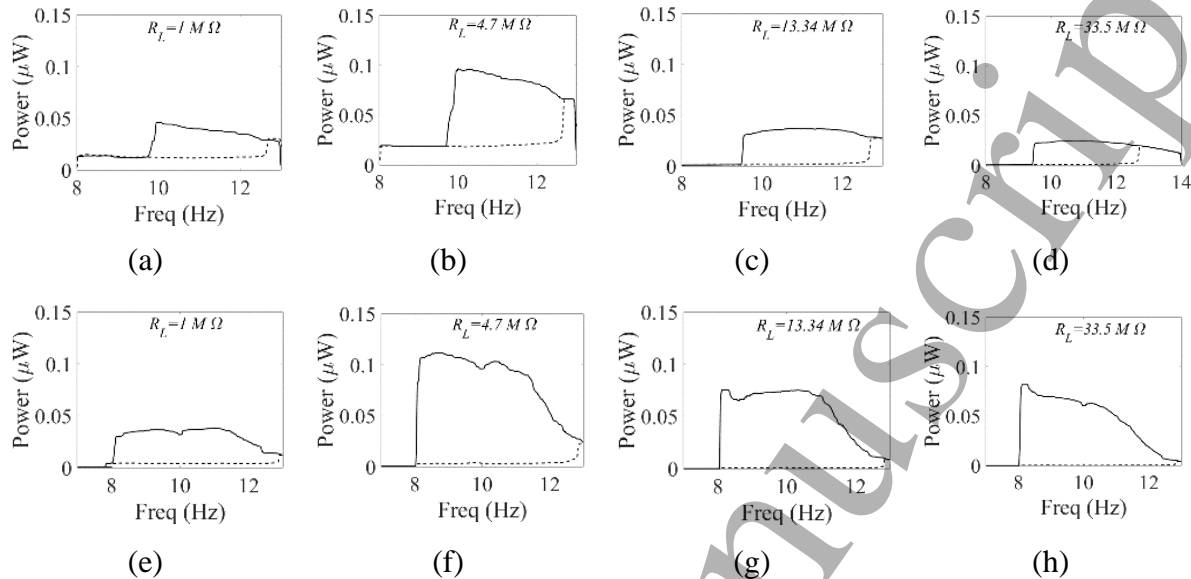

Figure 13. Power generation for the different load at 0.3g acceleration, (a)-(d) for Prototype 1; (e)-(h) for Prototype 2 (dashed line for forward sweeping, solid line for backward sweeping)

As shown in Figure 13, a larger power can be expected when the load resistance is 4.7 MΩ and the corresponding powers for Prototype 1 and Prototype 2 are 0.096 μW and 0.11 μW respectively. The generated power is limited by the energy conversion efficiency of the PVDF and the acceleration level. The results also show that the load resistance does not change the jumping frequencies of the SMSE/PVDF cantilever in the frequency responses, which indicates that the prototypes are weakly electromechanically coupled. This also explains the limited energy conversion efficiency.

6. Conclusions

In this paper, a smart material, soft magneto-sensitive elastomer, is proposed to broaden the frequency bandwidth of a PVDF vibrational energy harvester. Due to its soft and highly magneto-sensitive properties, the SMSE layer gives the harvester an obvious softening effect even at low acceleration levels. The difference between backward and forward jumping frequencies at 0.3 g acceleration for the Prototype 1 and Prototype 2 are 2.39 Hz and 4.34 Hz respectively. The 'force valley' effect of SMSE/PVDF-VEH is revealed, which leads to an interesting hardening effect with certain magnet dimensions and cantilever-PM gaps. The

23

power generated with different loads is plotted and the average power generated around the backward jumping frequencies are 0.096 μW and 0.11 μW for Prototype 1 and Prototype 2 respectively with a 4.7 MΩ load resistance. Future works will concentrate on improving the energy conversion efficiency of the SMSE cantilever based vibrational energy harvesters.

References

[1] Tao, K, L Tang, J Wu, S W Lye, H Chang and J Miao 2018 Investigation of Multimodal Electret-Based MEMS Energy Harvester With Impact-Induced Nonlinearity. *Journal of Microelectromechanical Systems* **27** 276 - 288

[2] Wang, W, J Cao, N Zhang, J Lin and W-H Liao 2017 Magnetic-spring based energy harvesting from human motions: Design, modeling and experiments. *Energy Conversion and Management* **132** 189-197

[3] Seveno, R, J Carbajo, T Dufay, B Guiffard and J C Thomas 2017 Flexible PET/Al/PZT/Al/PET multi-layered composite for low frequency energy harvesting. *Journal of Physics D: Applied Physics* **50** 165502

[4] Nour, E S, O Nur and M Willander 2017 Zinc oxide piezoelectric nano-generators for low frequency applications. *Semiconductor Science and Technology* **32** 064005

[5] Deng, J, K Rorschach, E Baker, C Sun and W Chen 2015 Topology optimization and fabrication of low frequency vibration energy harvesting microdevices. *Smart Materials and Structures* **24** 025005

[6] Naifar, S, S Bradai, C Viehweger and O Kanoun 2017 Survey of electromagnetic and magnetoelectric vibration energy harvesters for low frequency excitation. *Measurement* **106** 251-263

[7] Mitcheson, P D, E M Yeatman, G K Rao, A S Holmes and T C Green 2008 Energy harvesting from human and machine motion for wireless electronic devices. *Proceedings of the IEEE* **96** 1457-1486

[8] Halim, M A, H Cho and J Y Park 2015 Design and experiment of a human-limb driven, frequency up-converted electromagnetic energy harvester. *Energy Conversion and Management* **106** 393-404

[9] Izadgoshasb, I, Y Y Lim, N Lake, L Tang, R V Padilla and T Kashiwao 2018 Optimizing orientation of piezoelectric cantilever beam for harvesting energy from human walking. *Energy Conversion and Management* **161** 66-73

[10] Tang, L, Y Yang and C K Soh 2013 *Advances in Energy Harvesting Methods* (Springer, 17-61

24

[11] Malaji, P and S Ali 2017 Magneto-mechanically coupled electromagnetic harvesters for broadband energy harvesting. *Applied Physics Letters* **111** 083901

[12] Barton, D A W, S G Burrow and L R Clare 2010 Energy Harvesting From Vibrations With a Nonlinear Oscillator. *Journal of Vibration and Acoustics* **132** 021009-021009-021007

[13] Yang, W and S Towfighian 2017 Internal resonance and low frequency vibration energy harvesting. *Smart Materials and Structures* **26** 095008

[14] Leadenham, S and A Erturk 2015 Nonlinear M-shaped broadband piezoelectric energy harvester for very low base accelerations: primary and secondary resonances. *Smart Materials and Structures* **24** 055021

[15] Mohamed, B, A-R Eihab and S Mostafa 2016 Wideband, low-frequency springless vibration energy harvesters: part I. *Journal of Micromechanics and Microengineering* **26** 115021

[16] Baur, C, D J Apo, D Maurya, S Priya and W Voit 2014 *Polymer composites for energy harvesting, conversion, and storage* (ACS Publications, 1-27

[17] Qi, Y, J Kim, T D Nguyen, B Lisko, P K Purohit and M C McAlpine 2011 Enhanced Piezoelectricity and Stretchability in Energy Harvesting Devices Fabricated from Buckled PZT Ribbons. *Nano Letters* **11** 1331-1336

[18] Jiang, Y, S Shiono, H Hamada, T Fujita, K Higuchi and K Maenaka 2010 Low-frequency energy harvesting using a laminated PVDF cantilever with a magnetic mass. *Power MEMS* **2010** 375378

[19] Rocha, J G, L M Goncalves, P F Rocha, M P Silva and S Lanceros-Mendez 2010 Energy Harvesting From Piezoelectric Materials Fully Integrated in Footwear. *IEEE Transactions on Industrial Electronics* **57** 813-819

[20] Emad, A, M A E Mahmoud, M Ghoneima and M Dessouky, Modeling and analysis of stretching strain in clamped-clamped beams for energy harvesting.2016 *2016 IEEE 59th International Midwest Symposium on Circuits and Systems (MWSCAS)* 1-4

[21] Li, S, A Crovetto, Z Peng, A Zhang, O Hansen, M Wang, X Li and F Wang 2016 Bi-resonant structure with piezoelectric PVDF films for energy harvesting from random vibration sources at low frequency. *Sensors and Actuators A: Physical* **247** 547-554

[22] Zou, H-X, W-M Zhang, W-B Li, K-X Wei, K-M Hu, Z-K Peng and G Meng 2018 Magnetically coupled flextensional transducer for wideband vibration energy harvesting: Design, modeling and experiments. *Journal of Sound and Vibration* **416** 55-79

25

[23] Xia, H, R Chen and L Ren 2017 Parameter tuning of piezoelectric–electromagnetic hybrid vibration energy harvester by magnetic force: Modeling and experiment. *Sensors and Actuators A: Physical* **257** 73-83

[24] Jahani, K, M M Rafiei and P Aghazadeh 2017 How joint characteristics between a piezoelectric beam and the main structure affect the performance of an energy harvester. *Smart Materials and Structures* **26** 094004

[25] Wang, H and L Tang 2017 Modeling and experiment of bistable two-degree-of-freedom energy harvester with magnetic coupling. *Mechanical Systems and Signal Processing* **86** 29-39

[26] Lan, C, L Tang, W Qin and L Xiong 2017 Magnetically coupled dual-beam energy harvester: Benefit and trade-off. *Journal of Intelligent Material Systems and Structures* 1045389X17730927

[27] Ferrari, M, M Baù, M Guizzetti and V Ferrari 2011 A single-magnet nonlinear piezoelectric converter for enhanced energy harvesting from random vibrations. *Sensors and Actuators A: Physical* **172** 287-292

[28] Gou, X, Y Yang and X Zheng 2004 Analytic expression of magnetic field distribution of rectangular permanent magnets. *Applied Mathematics and Mechanics* **25** 297-306

[29] Erturk, A and D J Inman 2008 Issues in mathematical modeling of piezoelectric energy harvesters. *Smart Materials and Structures* **17** 065016

[30] Erturk, A and D J Inman 2008 On Mechanical Modeling of Cantilevered Piezoelectric Vibration Energy Harvesters. *Journal of Intelligent Material Systems and Structures* **19** 1311-1325

[31] Gunakala, S R, D M G Comissiong, K.Jordan and A Sankar 2012 A Finite Element Solution of the Beam Equation via MATLAB. *International Journal of Applied Science and Technology* **2** 80-88

[32] Low, T S and W Guo 1995 Modeling of a three-layer piezoelectric bimorph beam with hysteresis. *Journal of Microelectromechanical Systems* **4** 230-237

[33] Daqaq, M F, R Masana, A Erturk and D D Quinn 2014 On the role of nonlinearities in vibratory energy harvesting: a critical review and discussion. *Applied Mechanics Reviews* **66** 040801